

# Heterometallic Ce<sup>IV</sup>/V<sup>V</sup> Oxo Clusters with Adjustable Catalytic Reactivities

Xingjie Wang, Kieran Brunson, Haomiao Xie, Ian Colliard, Megan C. Wasson, Xinyi Gong, Kaikai Ma, Yufang Wu, Florencia A. Son, Karam B. Idrees, Xuan Zhang, Justin M. Notestein, May Nyman,\* and Omar K. Farha\*



Cite This: *J. Am. Chem. Soc.* 2021, 143, 21056–21065



Read Online

ACCESS |

Metrics & More

Article Recommendations

Supporting Information

**ABSTRACT:** Heterometallic Ce<sup>IV</sup>/M oxo clusters are underexplored yet and can benefit from synergistic properties from combining cerium and other metal cations to produce efficient redox catalysts. Herein, we designed and synthesized a series of new Ce<sub>12</sub>V<sub>6</sub> oxo clusters with different capping ligands: Ce<sub>12</sub>V<sub>6</sub>-SO<sub>4</sub>, Ce<sub>12</sub>V<sub>6</sub>-OTs (OTs: toluenesulfonic acid), and Ce<sub>12</sub>V<sub>6</sub>-NBSA (NBSA: nitrobenzenesulfonic acid). Single crystal X-ray diffraction (SCXRD) for all three structures reveals a Ce<sub>12</sub>V<sub>6</sub> cubane core formulated [Ce<sub>12</sub>(VO)<sub>6</sub>O<sub>24</sub>]<sup>18+</sup> with cerium on the edges of the cube, vanadyl capping the faces, and sulfate on the corners. While infrared spectroscopy (IR), ultraviolet-visible spectroscopy (UV-vis), electrospray ionization mass spectrometry (ESI-MS), and proton nuclear magnetic resonance (<sup>1</sup>H NMR) proved the successful coordination of the organic ligands to the Ce<sub>12</sub>V<sub>6</sub> core, liquid phase <sup>51</sup>V NMR and small-angle X-ray scattering (SAXS) confirmed the integrity of the clusters in the organic solutions. Furthermore, functionalization of the Ce<sub>12</sub>V<sub>6</sub> core with organic ligands both provides increased solubility in term of homogeneous application and introduces porosity to the assemblies of Ce<sub>12</sub>V<sub>6</sub>-OTs and Ce<sub>12</sub>V<sub>6</sub>-NBSA in term of heterogeneous application, thus allowing more catalytic sites to be accessible and improving reactivity as compared to the nonporous and less soluble Ce<sub>12</sub>V<sub>6</sub>-SO<sub>4</sub>. Meanwhile, the coordinated ligands also influenced the electronic environment of the catalytic sites, in turn affecting the reactivity of the cluster, which we probed by the selective oxidation of 2-chloroethyl ethyl sulfide (CEES). This work provides a strategy to make full use of the catalytic sites within a class of inorganic sulfate capped clusters *via* organic ligand introduction.



## INTRODUCTION

Metal oxide nanomaterials are attractive for a variety of applications including catalysis,<sup>1,2</sup> drug delivery,<sup>3,4</sup> photochemistry,<sup>5</sup> sensing,<sup>6</sup> and optoelectronics.<sup>7,8</sup> In addition to potentially enhanced properties, structurally well-defined nanosized oxides can offer a platform to precisely interrogate structure–activity relationships. Therefore, scientists have systematically investigated the properties/activities including conductivity, thermal stability, magnetic behavior, and catalytic performance of the metal oxides with varied surface and/or interface-tuning approaches through regulating the exposed facets, chemical composition, morphology, size, and surface functional groups.<sup>9–14</sup>

For example, Zhang et al. reported that the band gaps of the Ti<sub>6</sub> complexes can be gradually reduced as the electron-withdrawing effect increases through varying the organic species, which significantly influences the photocatalytic performance. This ligand study included carboxylates, phosphonates, and sulfonates.<sup>15</sup> In addition to altering the electronics of metal oxide materials, surface ligands can affect the crystalline packing of the clusters. While densely packed metal oxide clusters confine the reaction to happen on

accessible surface sites, the introduction of porosity in the cluster assemblies exposes more active sites to the substrate. For example, a “Star of David”-shape heterometallic cluster Ni<sub>36</sub>Gd<sub>102</sub> was reported possessing a high BET area of ~300 m<sup>2</sup> g<sup>-1</sup>, which presented high reactivity in photocatalytic CO<sub>2</sub> reduction as a result of potential open metal sites with the CO<sub>2</sub> absorption ability.<sup>16</sup> Further, some of us have reported that different aromatic capping agents on Ce<sub>38</sub> cluster not only induced the porosity and the catalytic performance but also affected the intrinsic properties of the clusters comprising the lattice defect environment and mechanical stability.<sup>17</sup> The observation of these reported intriguing phenomena attracted our attention to investigate both the porosity and electronic effect resulting from the ligand introduction and variation,

Received: October 22, 2021

Published: December 7, 2021



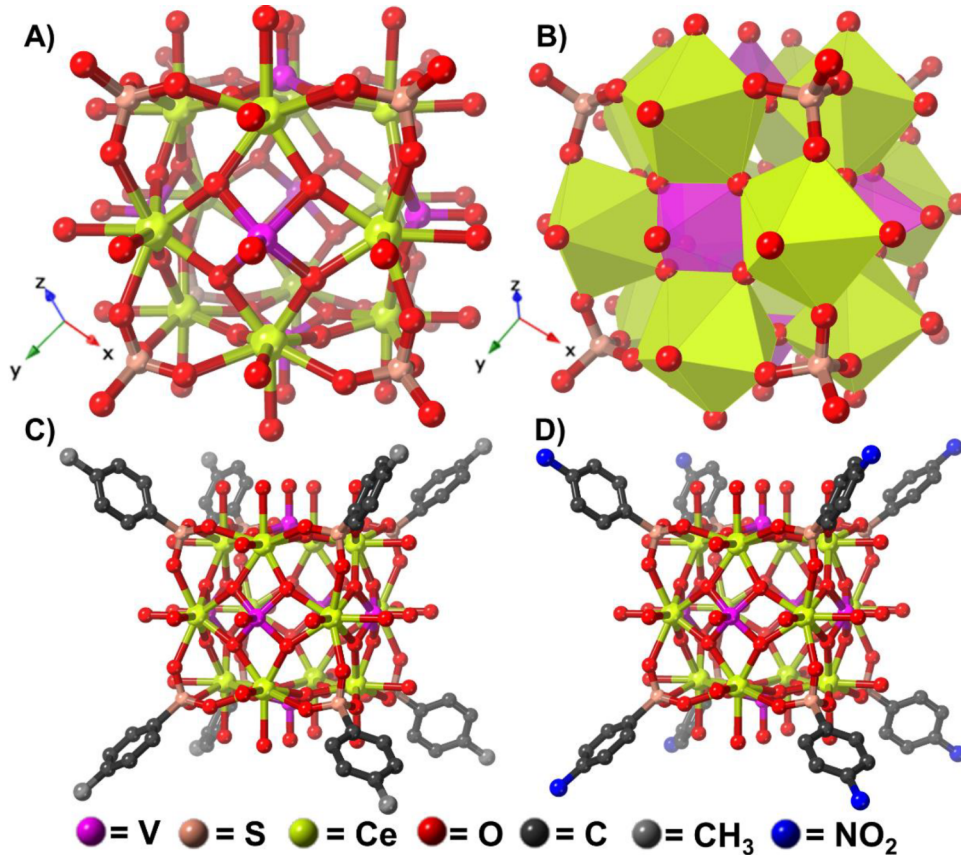


**Figure 1.** (A) Ball and stick structural mode for  $\text{Ce}_{12}\text{V}_6\text{-SO}_4$ . (B) Polyhedral mode for  $\text{Ce}_{12}\text{V}_6\text{-SO}_4$ . Ball and stick structural mode for (C)  $\text{Ce}_{12}\text{V}_6\text{-OTs}$  and (D)  $\text{Ce}_{12}\text{V}_6\text{-NBSA}$ .

which is still rarely discussed in metal-oxo cluster chemistry yet is significant for catalytic performance.

Ceria-based materials are ubiquitous within heterogeneous catalysis,<sup>14,18–24</sup> photocatalytic oxidation,<sup>17,25</sup> solar fuel,<sup>26–28</sup> and biomedical applications,<sup>29–31</sup> a function of the facile  $\text{Ce}^{\text{IV}}/\text{Ce}^{\text{III}}$  redox couple that enables the selective storage, release, and transport of oxygen. For instance, it was shown that active interfacial oxygen sites for propane activation formed upon introducing ceria to manganese oxide, creating a strong oxide–support interaction, thus tuning the catalysts to possess both high activity and propene selectivity.<sup>32</sup> Moreover, ceria has served as an efficient catalyst for water gas shift reaction<sup>33–35</sup> among other catalytic applications<sup>21</sup> due to the outstanding oxygen storage capacity as well as the ease in oxygen vacancies generation and reparation. To date, several examples exist of discrete  $\text{Ce}^{\text{IV}}/\text{M}$  oxo compounds, clusters, and polyoxometalates, which have been predominantly investigated for magnetic studies but few for catalysis.<sup>36–40</sup> Meanwhile, ceria-supported vanadium catalysts have demonstrated high potential in oxidative catalysis, like oxidative dehydrogenation,<sup>20,41</sup> cyclohexene epoxidation,<sup>42</sup> and methanol oxidation.<sup>43,44</sup> Therefore, developing and interrogating heterometallic  $\text{Ce}/\text{V}$ -oxo clusters for catalysis poses a great interest to both the catalytic and bimetallic  $\text{Ce}/\text{V}$  cluster field. Recently, a V polyoxovanadate,  $(n\text{-Bu}_4\text{N})_2[(\text{Ce}^{\text{III}}(\text{dmso})_3)_2\text{V}^{\text{IV}}\text{V}^{\text{V}}_{11}\text{O}_{33}\text{Cl}]$  with  $\text{Ce}^{\text{III}}$  dopants, and a cluster,  $\text{Ce}_4\text{V}_4\text{O}_{13}$ , were synthesized; these clusters were utilized for indigo degradation and thioanisole oxidation, respectively.<sup>45,46</sup> However, the aforementioned clusters resembled vanadium doped with cerium rather than bulk ceria, and these materials also formed extended crystals with no

internal porosity, limiting reactivity as a heterogeneous catalyst. To contribute efforts to the heterometallic  $\text{Ce}^{\text{IV}}/\text{M}$  oxo cluster field and provide a strategy on establishing porous clusters, we designed and synthesized a series of atomically precisely defined  $\text{Ce}/\text{V}$  clusters with high nuclearity and porosity and used them as a platform to study the surface chemistry and induced ligand effect.

In this work, we first report a  $\text{Ce}_{12}\text{V}_6$  oxo cluster capped with sulfate ligands,  $\text{Ce}_{12}\text{V}_6\text{-SO}_4$ , to yield a bridging  $\text{Ce}-\text{O}-\text{V}$  bond. The structure is highly symmetric, but owing to the dense nature of this inorganic cluster, it presents a limited porosity. We achieved a permanent porosity by forming another two isostructural  $\text{Ce}_{12}\text{V}_6$  oxo clusters,  $\text{Ce}_{12}\text{V}_6\text{-OTs}$  and  $\text{Ce}_{12}\text{V}_6\text{-NBSA}$ , which are capped with larger, aromatic sulfonate-based linkers, namely, toluenesulfonic acid (TsOH) and 4-nitrobenzenesulfonic acid (NBSA). The structure for each of the clusters was verified by a series of X-ray and spectroscopic techniques, and then, we interrogated the oxidative behavior of this cluster family with the selective catalytic oxidation of 2-chloroethyl ethyl sulfide (CEES). The clusters as catalysts displayed varied reactivities, giving the highest catalytic performance for  $\text{Ce}_{12}\text{V}_6\text{-OTs}$  among all the clusters, attributed to the introduced porosity and altering cluster electronics.

## RESULTS AND DISCUSSION

**Synthesis and Structural Discussion.** In this work, a  $\text{Ce}_{12}\text{V}_6\text{-SO}_4$  (Figure 1A,B) cluster was obtained by the assembly of  $\text{Ce}(\text{NH}_4)_2(\text{NO}_3)_6$ ,  $\text{VCl}_3$ , with sulfonic acid in aqueous condition. However, due to the dense packing within the crystal lattice of  $\text{Ce}_{12}\text{V}_6\text{-SO}_4$ , negligible void space is

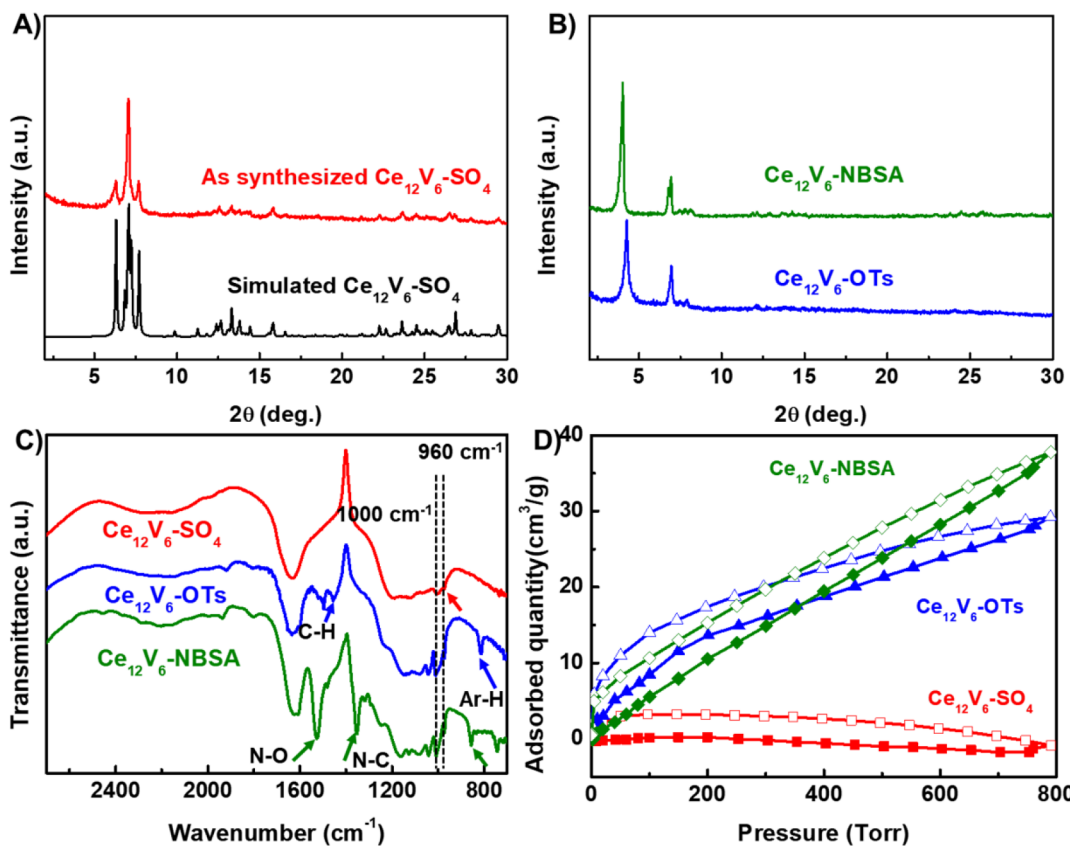


**Figure 2.** PXRD patterns of as-synthesized (A)  $\text{Ce}_{12}\text{V}_6\text{-SO}_4$ , compared to the simulated patterns and (B) extended clusters  $\text{Ce}_{12}\text{V}_6\text{-NBSA}$  and  $\text{Ce}_{12}\text{V}_6\text{-OTs}$ . (C) IR spectra and (D)  $\text{CO}_2$  adsorption at 195 K of the as-synthesized clusters.

presented, limiting the access of substrates to the active sites, thus hugely decreasing its envisioned catalytic applications. We sought to position this catalyst to be effective within homogeneous catalysis by increasing the solubility and within heterogeneous catalysis by introducing porous packing within the assembly. Thus, we chose two different sulfate-containing aromatic organic ligands for the cluster synthesis, toluene-sulfonic acid, and 4-nitrobenzenesulfonic acid to increase the solubility in common organic solvents and induce porosity. These two ligands feature para-substituted functional groups,  $-\text{CH}_3$  and  $-\text{NO}_2$ , which have opposite electronic effects to enable further control over the cluster's electronics. We modified the synthetic conditions for  $\text{Ce}_{12}\text{V}_6\text{-SO}_4$  to instead yield  $\text{Ce}_{12}\text{V}_6\text{-OTs}$  and  $\text{Ce}_{12}\text{V}_6\text{-NBSA}$  (Figure 1C,D). As seen from Figure S1, lowering the amount of ligand added resulted in the as-synthesized cluster,  $\text{Ce}_{12}\text{V}_6\text{-OTs-0.6}$  (where 0.6 represented the usage of 0.6 mL of 1 M TsOH solution for the synthesis), having poor crystallinity but a similar powder X-ray diffraction (PXRD) pattern as  $\text{Ce}_{12}\text{V}_6\text{-SO}_4$ . The structure of which was further confirmed by single crystal X-ray diffraction (SCXRD) to be the exact same as  $\text{Ce}_{12}\text{V}_6\text{-SO}_4$ . However, as a higher ligand concentration was applied, a new peak appeared at a lower degree and a better crystallinity was obtained. This result confirmed that  $\text{Ce}_{12}\text{V}_6\text{-OTs}$  possessed the same core as the  $\text{Ce}_{12}\text{V}_6\text{-SO}_4$ , and the appearance of the new peak can be related to the introduction of organic ligand.  $\text{Ce}_{12}\text{V}_6\text{-NBSA}$  was then synthesized on the basis of a similar synthetic procedure as  $\text{Ce}_{12}\text{V}_6\text{-OTs}$ .

Further structural insight of the clusters was explored by SCXRD analyses. As  $\text{Ce}_{12}\text{V}_6\text{-SO}_4$  crystallizes in the orthorhombic space group  $Pnma$  [ $a = 27.9928(10)$  Å,  $b =$

$24.9070(6)$  Å,  $c = 14.5659(3)$  Å], it sits at a mirror plane with six crystallographically independent Ce atoms, three V atoms, and four  $\text{SO}_4^{2-}$  ligands in an asymmetric unit to produce a cubane-like structure (Figure 1 and Table S1). All Ce atoms adopt an eight-coordinate dodecahedral geometry and locate at 12 edges of the cube. With Ce—O bond lengths ranging within 2.1–2.6 Å, the cluster features two free Ce—O (oxygen atoms from water molecules), two Ce—O—S, and four Ce—O—V(Ce) bonds. The vanadyl are square-pyramidal and located in the center of six faces of the cube, bridging to four Ce via oxo ligands. The terminal V=O have bond lengths ranging from 1.5 to 1.7 Å. The V—O(—Ce) bonds are 1.7–2.0 Å. It is noted that, though most of the V=O ( $V_{\text{out}}$ ) bonds face vertically out of the surface, there is a disordered V atom ( $V_{\text{in}}$ ) facing into the cavity with an occupancy of 0.5, giving a ratio of 5.5 to 0.5 for  $V_{\text{out}}/V_{\text{in}}$  (Figure S2). In addition to the Ce and V atoms located on each edge and face of the cubane cluster, respectively, sulfates sit in the eight corners, with the S—O distances ranging from 1.4 to 1.6 Å. As a highly symmetric and well-organized cluster, it presents a unique assembly of metal doping on the surface of Ce oxo cluster. Given all provided information above and further characterization with inductively coupled plasma optical emission spectroscopy (ICP-OES) and X-ray photoelectron spectroscopy (XPS), which calculated the ratio of Ce/V/S and verified the valence of Ce and V (*vide infra*), the formula of  $\text{Ce}_{12}\text{V}_6\text{-SO}_4$  cluster was assigned as  $[\text{Ce}^{\text{IV}}_{12}(\text{V}^{\text{V}}\text{O})_6\text{O}_{24}(\text{H}_2\text{O})_{24}(\text{SO}_4)_8]^{2+}$  with a formal 2+ charge, which was balanced with one outer sphere anion  $\text{SO}_4^{2-}$  as the counterion.

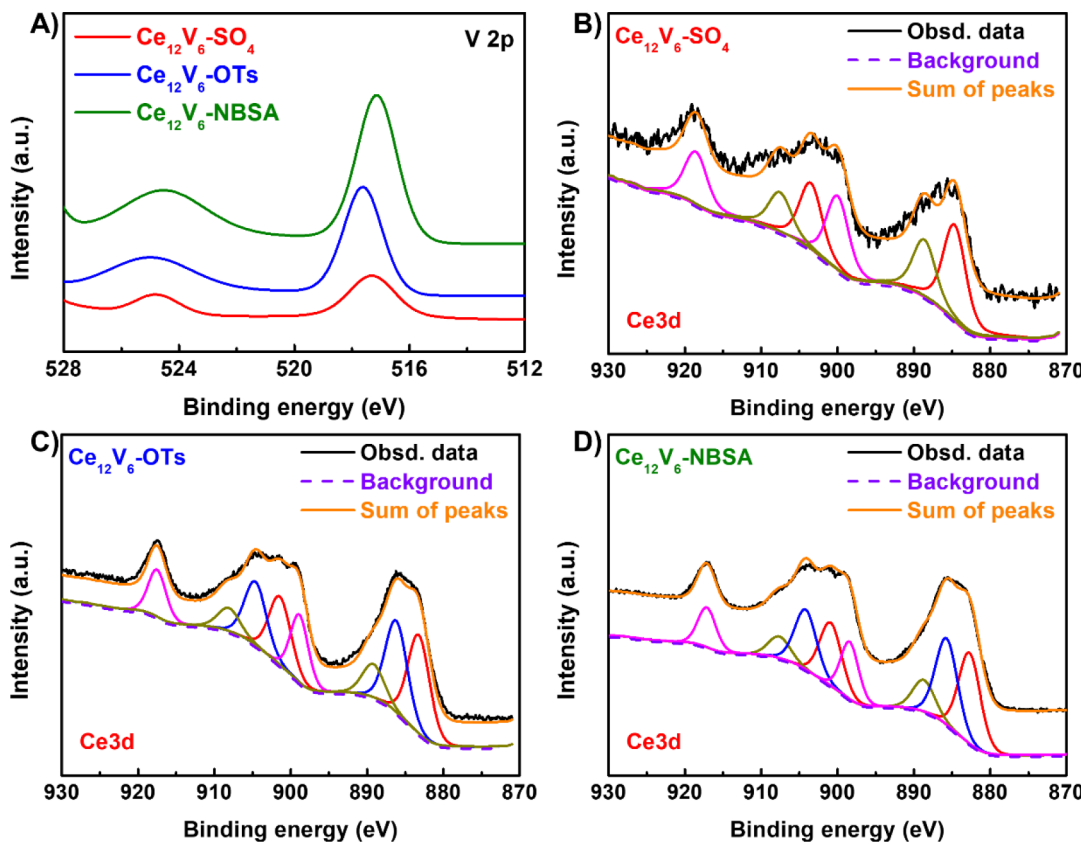


**Figure 3.** (A) V 2p XPS spectra comparison among as-synthesized  $\text{Ce}_{12}\text{V}_6$  clusters. Ce 3d XPS spectra of (B)  $\text{Ce}_{12}\text{V}_6\text{-SO}_4$ , (C)  $\text{Ce}_{12}\text{V}_6\text{-OTs}$ , and (D)  $\text{Ce}_{12}\text{V}_6\text{-NBSA}$ . Blue lines in Ce 3d spectra represent  $\text{Ce}^{3+}$ -related peaks.

A modified synthetic protocol was utilized for  $\text{Ce}_{12}\text{V}_6\text{-OTs}$  and  $\text{Ce}_{12}\text{V}_6\text{-NBSA}$  (see the *Supporting Information (SI)* for more details). While *in situ* single crystal generation from the mother solution gave the exact same structure as  $\text{Ce}_{12}\text{V}_6\text{-SO}_4$ , confirmed by SCXRD, it suggested a breakage of C–S bond on the organic ligands during the synthesis, likely due to the strong oxidizing ( $\text{Ce}^{4+}/\text{Ce}^{3+}$  from  $\text{Ce}^{\text{IV}}$  salts) and acidic ( $\text{pH} < 1$ ) synthetic environment.<sup>47</sup> Attention was then mainly paid to another strategy—recrystallization. We obtained a  $\sim 100 \mu\text{m}$  octahedral single crystal with round edges *via* diethyl ether (DEE) diffusion into the  $\text{Ce}_{12}\text{V}_6\text{-OTs}$  and  $\text{Ce}_{12}\text{V}_6\text{-NBSA}$  *N,N*-dimethylformamide (DMF)/ dimethoxyethane (DME) mixed solution (see the *Supporting Information* for more details). The structure was later collected and solved by SCXRD, showing that the compound crystallizes in a cubic  $F\bar{m}\bar{3}m$  space group [ $a = 26.7362(2) \text{ \AA}$ ] (Table S1). With the consistent  $\text{Ce}_{12}\text{V}_6$ -oxo core, we did not directly observe the organic ligands but were able to model in two ligands per  $\text{Ce}_{12}\text{V}_6$ -oxo core due to the enlarged space among the discrete clusters (Figure S3A,B) as well as the presence of the ligands confirmed by the  $^1\text{H}$  NMR measurement from the same batch single crystal (Figure S4). Of note, there are 24 DMF molecules with disordered orientation coordinated to the Ce centers by substituting all the terminal  $\text{H}_2\text{O}$  molecules after the recrystallization process (Figure S3C,D). Combined, they indicate that DMF is not a good solvent system for recrystallization in this particular case because its alkaline and reducing characters likely break the C–S bond in the cluster (*vide supra*). While other solvent systems failed to give any single crystals, the DEE/(DMF+DME) system confirmed the isostructural nature of these three clusters. The formulas

for the as-synthesized  $\text{Ce}_{12}\text{V}_6\text{-OTs}$  and  $\text{Ce}_{12}\text{V}_6\text{-NBSA}$  powder were then confirmed by proton nuclear magnetic resonance ( $^1\text{H}$  NMR), ICP-OES, and XPS (*vide infra*) to be  $[\text{Ce}^{\text{IV}}_9\text{Ce}^{\text{III}}_3(\text{V}^{\text{V}}\text{O})_6\text{O}_{24}(\text{H}_2\text{O})_{21}(\text{OH})_3(\text{SO}_4)(\text{OTs})_7]^{3+}$  and  $[\text{Ce}^{\text{IV}}_9\text{Ce}^{\text{III}}_3(\text{V}^{\text{V}}\text{O})_6\text{O}_{24}(\text{H}_2\text{O})_{21}(\text{OH})_3(\text{SO}_4)_2(\text{NBSA})_6]^{2+}$ , which are balanced with 1.5 and 1 anion  $\text{SO}_4^{2-}$  as the counterion.

**Characterization.** The as-synthesized clusters were fully characterized both in the solid state and in solution. PXRD results confirmed the phase purity as highly consistent patterns were observed as compared to their simulated counterparts and analogues (Figure 2A,B).

While the first peak appeared at  $6.30^\circ 2\theta$  for  $\text{Ce}_{12}\text{V}_6\text{-SO}_4$  (Figure 2A), the peak shifted to lower angles to  $4.2$  and  $4.0^\circ 2\theta$  for  $\text{Ce}_{12}\text{V}_6\text{-OTs}$  and  $\text{Ce}_{12}\text{V}_6\text{-NBSA}$ , respectively, due to the increased *d*-spacing from  $14.03$  to  $21.04$  and  $22.09 \text{ \AA}$ , resulting from the ligand introduction (Figure 2B). A slight difference of  $\sim 0.2^\circ 2\theta$  ( $\sim 1 \text{ \AA}$  for *d*-spacing) between the first peak for  $\text{Ce}_{12}\text{V}_6\text{-OTs}$  and  $\text{Ce}_{12}\text{V}_6\text{-NBSA}$  was rationalized as a result of the larger size of the  $-\text{NO}_2$  group than the  $-\text{CH}_3$  group. To further verify the structure, ICP-OES quantified the ratio of Ce to V in the clusters. As shown in the Table S2, all clusters possessed a similar ratio of around 2–1 for Ce/V, with approximately 9 S per  $\text{Ce}_{12}\text{V}_6$  core (8.6, 9.2, and 8.7 for  $\text{Ce}_{12}\text{V}_6\text{-SO}_4$ ,  $\text{Ce}_{12}\text{V}_6\text{-OTs}$ , and  $\text{Ce}_{12}\text{V}_6\text{-NBSA}$ , respectively), suggesting that 1 or 1.5 uncoordinated  $\text{SO}_4^{2-}$  was trapped in the bulk materials. While scanning electron microscopy (SEM) showed a plate morphology with a similar size around  $2\text{--}4 \mu\text{m}$  (Figure S5A,C,E), the energy dispersive X-ray spectroscopy (EDS) line scan showed that Ce and V were distributed evenly throughout the whole crystal with an atom ratio of about 2:1

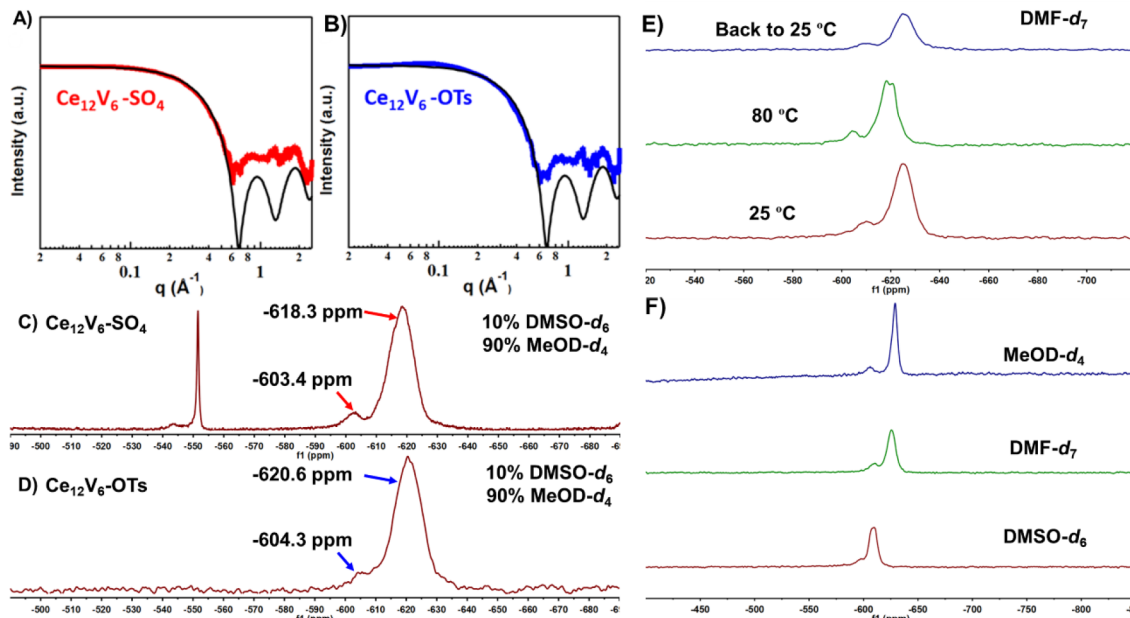


**Figure 4.** SAXS curves for (A)  $\text{Ce}_{12}\text{V}_6\text{-SO}_4$  and (B)  $\text{Ce}_{12}\text{V}_6\text{-OTs}$  (the mismatch between experimental and simulated data between  $q = 0.06\text{--}0.2 \text{\AA}^{-1}$  is a structure factor, due to the higher concentration of the  $\text{Ce}_{12}\text{V}_6\text{-OTs}$  solution). Simulated scattering is shown in black with a good match to experimental scattering. Liquid phase  $^{51}\text{V}$  NMR of (C)  $\text{Ce}_{12}\text{V}_6\text{-SO}_4$  and (D)  $\text{Ce}_{12}\text{V}_6\text{-OTs}$  in  $\text{DMSO-}d_6\text{/MeOD-}d_4$  (10%, v/v) mixture solution. Noted, the sharp peak, which was only observed in  $\text{Ce}_{12}\text{V}_6\text{-SO}_4$ , is likely an orthovanadate impurity with a ratio of ~8%. The  $^{51}\text{V}$  NMR spectra of (E)  $\text{Ce}_{12}\text{V}_6\text{-OTs}$  in  $\text{DMF-}d_7$  with increased temperature and (F)  $\text{Ce}_{12}\text{V}_6\text{-OTs}$  in different solvents.

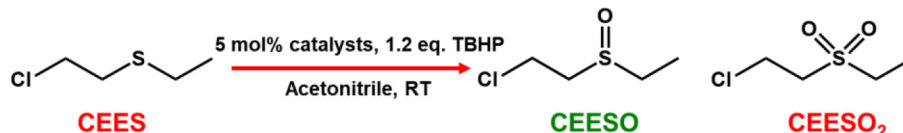
(Figure S5B,D,F and Table S3), in accordance with the ICP results. Furthermore, microtome-cut  $\text{Ce}_{12}\text{V}_6\text{-OTs}$  crystals were examined, as a representative example, through high-resolution transmission electron microscopy (HRTEM). TEM images of  $\text{Ce}_{12}\text{V}_6\text{-OTs}$  (Figure S6) directly revealed lattice spacing of 2.1 nm, consistent with the increased  $d$ -spacing from PXRD, which further confirmed the introduction of OTs capping ligands.

The presence of ligands in  $\text{Ce}_{12}\text{V}_6\text{-OTs}$  and  $\text{Ce}_{12}\text{V}_6\text{-NBSA}$  was then verified by proton NMR and the amount of ligands was quantified by using mesitylene as an internal standard to give ~7 TsOH and ~6 NBSA per  $\text{Ce}_{12}\text{V}_6$  core, respectively (Figure S7). The attempt to obtain fully organic ligand coordination (eight TsOH/NBSA per core) was unsuccessful in our lab as a result of the harsh synthetic condition (*vide supra*). Infrared spectroscopy (IR) was then applied to further support the coordinated state. As shown in Figure 2C, all clusters exhibited a similar band at around  $960 \text{ cm}^{-1}$ , which can be assigned to the S—O(—M) bond, indicating the successful ligand insertion with a coordination bond.<sup>48</sup> The peak located at around  $1000 \text{ cm}^{-1}$ , which was observed for all samples, can be assigned to the terminal V=O stretches.<sup>39</sup> For  $\text{Ce}_{12}\text{V}_6\text{-OTs}$ , the peaks at  $813$  and  $1450 \text{ cm}^{-1}$  represented the aromatic C—H bending and C—H bending of the —CH<sub>3</sub> group, respectively. In the case of  $\text{Ce}_{12}\text{V}_6\text{-NBSA}$ , there are three major stretching bands at around  $1527$ ,  $1350$ , and  $856 \text{ cm}^{-1}$ , which correspond to N—O and N—C stretches as well as aromatic C—H bending.<sup>49</sup> We then explored solid-state ultraviolet-visible (UV-vis) spectroscopy of the clusters to explore the clusters' light absorption property. All clusters displayed strong light absorption ability in the UV region with a slightly broader absorption range to  $552/540 \text{ nm}$  for  $\text{Ce}_{12}\text{V}_6\text{-OTs}/\text{Ce}_{12}\text{V}_6\text{-NBSA}$  than the  $506 \text{ nm}$  for the  $\text{Ce}_{12}\text{V}_6\text{-SO}_4$  (Figure S8), which can be ascribed to the coordinated ligands that influence the structure. Furthermore, electrospray ionization mass spectrometry (ESI-MS) was also carried out

in a methanol solution of  $\text{Ce}_{12}\text{V}_6\text{-OTs}$  in a positive mode (Figure S9). The obtained result is highly consistent with the chemical formula that has been proposed, giving only a negligible mismatch likely resulting from the loss of protons. With the above characterizations, we concluded the successful synthesis of the bulk materials with aromatic ligands.

After confirming the synthesis of isostructural  $\text{Ce}_{12}\text{V}_6$  clusters with NBSA and OTs capping ligands, we probed the resulting porosity among the clusters. CO<sub>2</sub> sorption measurements at 195 K demonstrated an enhanced CO<sub>2</sub> uptake for  $\text{Ce}_{12}\text{V}_6\text{-OTs}$  and  $\text{Ce}_{12}\text{V}_6\text{-NBSA}$  with a respective BET area of ~70 and ~80 m<sup>2</sup>/g, while  $\text{Ce}_{12}\text{V}_6\text{-SO}_4$  exhibited no porosity (Figure 2D), indicating the successful introduction of porosity in the cluster assemblies with the bulkier sulfate linkers. Such an increased surface area is beneficial for heightened substrate access to the active sites. Thermal gravimetric analysis (TGA) under air suggested that  $\text{Ce}_{12}\text{V}_6\text{-SO}_4$  was stable up to 700 °C while  $\text{Ce}_{12}\text{V}_6\text{-OTs}$  and  $\text{Ce}_{12}\text{V}_6\text{-NBSA}$  suffered ligand decomposition beginning around 400 °C (Figure S9A). Meanwhile, variable-temperature PXRD confirmed the retained crystallinity under a high temperature (100 °C) (Figure S9B,C). Next, we used XPS to characterize the oxidation states. As shown in Figure 3A and Figure S10, all clusters contained V<sup>5+</sup> species yet exhibited notable binding energy (B.E.) differences. We observed the highest V 2p<sub>3/2</sub> B.E. of 517.7 eV in  $\text{Ce}_{12}\text{V}_6\text{-OTs}$  and the lowest V 2p<sub>3/2</sub> B.E. of 517.1 eV in  $\text{Ce}_{12}\text{V}_6\text{-NBSA}$  (Table S4), while  $\text{Ce}_{12}\text{V}_6\text{-SO}_4$  had an intermediate B.E. of 517.3 eV. We attribute this difference in B.E. to the divergent coordination environment as a result of the diverse capping ligands.<sup>50–52</sup> Moreover, XPS probed the Ce oxidation states among the clusters;  $\text{Ce}_{12}\text{V}_6\text{-SO}_4$  contained only Ce<sup>4+</sup> while  $\text{Ce}_{12}\text{V}_6\text{-OTs}$  and  $\text{Ce}_{12}\text{V}_6\text{-NBSA}$  contained ~25% Ce<sup>3+</sup> on the basis of the integrated area of Ce<sup>3+</sup>-related peaks at 886.3/409.8 eV ( $\text{Ce}_{12}\text{V}_6\text{-OTs}$ ) and 885.9/904.4 eV ( $\text{Ce}_{12}\text{V}_6\text{-NBSA}$ ) (Figure 3B–D). The generation of Ce<sup>3+</sup> species compared to

Scheme 1. Reaction Scheme for CEES Oxidation



the inorganic  $\text{Ce}_{12}\text{V}_6\text{-SO}_4$  could be interpreted by the excess addition of organic ligands, of which the C–S bond would be broken (*vide supra*) and get oxidized by the  $\text{Ce}^{4+}$  during the reaction, resulting the generation of the reduced Ce species.

We further probed their properties in solution phase. In the absence of any organic components,  $\text{Ce}_{12}\text{V}_6\text{-SO}_4$  can be considered as an inorganic metal oxide with demonstrated poor solubility, presenting only mild to low solubility in neat straight-chain amines (but likely with decomposition) and 10% (v/v) dimethyl sulfoxide (DMSO)-methanol (MeOH). With the introduction of organic ligands to the cluster, a higher solubility was achieved for  $\text{Ce}_{12}\text{V}_6\text{-OTs}$  and  $\text{Ce}_{12}\text{V}_6\text{-NBSA}$  in DMF, DMSO, MeOH, N-methyl-2-pyrrolidone (NMP), and dimethylacetamide (DMA) at room temperature (>50 mg/mL), while they remain insoluble in acetone, acetonitrile, and dichloromethane. Of note, both  $\text{Ce}_{12}\text{V}_6\text{-OTs}$  and  $\text{Ce}_{12}\text{V}_6\text{-NBSA}$  were largely insoluble when modified synthetic conditions incorporated lower than four ligands per  $\text{Ce}_{12}\text{V}_6$  core. Given our observations of the high solubility in a range of organic solvents, we first utilized dynamic light scattering (DLS) to interrogate the cluster size in solution as to confirm its structural integrity.  $\text{Ce}_{12}\text{V}_6\text{-OTs}$  and  $\text{Ce}_{12}\text{V}_6\text{-SO}_4$  were then chosen for the following studies. Upon dissolution in DMF,  $\text{Ce}_{12}\text{V}_6\text{-OTs}$  exhibited an average size of ~2 nm (Figure S11A), consistent with the simulated perfect size of the discrete cluster (Figure S11B), indicating that the structure remained intact in the solution phase. Small angle X-ray scattering (SAXS) curves also confirmed the presence of intact  $\text{Ce}_{12}\text{V}_6$  clusters in solution upon dissolution of the crystalline materials as the simulated scattering match well with the experimental scattering through the Guinier region of the scattering curves ( $q < 0.5 \text{ \AA}^{-1}$ , Figure 4A,B). For both experimental scattering curves, even the oscillations at  $q > 0.5 \text{ \AA}^{-1}$  are observable, albeit somewhat obstructed by solvent scattering. Observations of oscillations in addition to the excellent match between simulated and experimental scattering is a testament to the monodispersity and structural integrity of the clusters in solution. A structure factor in the scattering curve would occur at lower angles and be present as either a positive or negative deviation from the horizontal plateau. The scattering data did not exhibit such deviation within the early Guinier region, meaning that we did not observe a structure factor. This in turn indicated little to no Coulombic forces between scatterers in solution, which we attribute to the low-valence of the  $\text{Ce}_{12}\text{V}_6$  oxo clusters.

The integrity of the cluster was further corroborated by liquid phase  $^{51}\text{V}$  NMR. While the  $^{51}\text{V}$  NMR spectra in  $\text{DMSO-d}_6/\text{MeOD-d}_4$  (10%, v/v) presented one major peak at  $-620.6$  and  $-618.3$  ppm for  $\text{Ce}_{12}\text{V}_6\text{-OTs}$  and  $\text{Ce}_{12}\text{V}_6\text{-SO}_4$ , respectively, a small peak at around  $-604$  ppm was also observed in both spectra (Figure 4C,D). The small peak was then assigned to the disordered vanadium facing into the cavity ( $\text{V}_{\text{in}}$ ) with the major peak delegation of the outward vanadium facing to the outer surface ( $\text{V}_{\text{out}}$ ), as the integration area ratios were highly consistent with our structure disorder ratio (*vide supra*).

(Figures S12 and S13). Combined, the results demonstrated the structural integrity in the solution. In addition, the identical  $^{51}\text{V}$  spectra of  $\text{Ce}_{12}\text{V}_6\text{-OTs}$  to  $\text{Ce}_{12}\text{V}_6\text{-SO}_4$  further verified their isostructural nature.

Given the presence of one anomalous vanadium disorder to the others, we further investigated this disorder with in-depth liquid phase  $^{51}\text{V}$  NMR studies to determine the origin of this unexpected disorder and its effect on solution phase integrity of the cluster. Here we consider both temperature and solvent. The variable-temperature  $^{51}\text{V}$  spectra indicate that a high temperature would increase disorder to the  $\text{V}_{\text{out}}$  species but show reduction on the  $\text{V}_{\text{in}}$ , while low-temperature results presented an opposed phenomenon with increased  $\text{V}_{\text{in}}$  disorders (Figure 4E, Figure S14A–C, and Tables S5 and S6). The variation of disorder by differentiating the temperatures can be rationalized with the reorientation of the nearby molecules around the vanadium species.<sup>53</sup> Though a decreased  $\text{V}_{\text{in}}$  was observed at high temperature, it came back when cooling to room temperature (Figure 4E and Figure S14B). In terms of solvent effects, three solvents (DMF- $d_7$ , MeOD- $d_4$ , and DMSO- $d_6$ ) were utilized for dissolution and  $^{51}\text{V}$  NMR of  $\text{Ce}_{12}\text{V}_6\text{-OTs}$ , given its greater flexibility in dissolution compared to  $\text{Ce}_{12}\text{V}_6\text{-SO}_4$  (Figure 4F). The  $^{51}\text{V}$  spectra in MeOD- $d_4$  and DMF- $d_7$  exhibit a well-defined  $\text{V}_{\text{in}}$  peak, in addition to the  $\text{V}_{\text{out}}$  peak. In DMSO- $d_6$ , however, the  $\text{V}_{\text{in}}$  peak is a shoulder to the  $\text{V}_{\text{out}}$  peak. We hypothesize that the ability for these coordinating solvents to bind both vanadium and cerium increases as methanol < DMF < DMSO (Table S7). Structural evidence shows the favorable bonding of DMSO to both V and Ce in oxo-clusters.<sup>54,55</sup> Therefore, DMSO can stabilize the  $\text{V}_{\text{out}}$ , promoting an exchange between  $\text{V}_{\text{out}}$  and  $\text{V}_{\text{in}}$  while pure methanol simply does not promote exchange, providing the clearest separation of  $\text{V}_{\text{out}}$  and  $\text{V}_{\text{in}}$ . Interestingly, a serial introduction of DMSO into methanol illustrates a emergence of two peaks (Figure S14E), yet this seemingly occurs without losing the structural integrity of the cluster. The result can then be well-understood by the chemical shifts due to the solvent effect,<sup>56,57</sup> resulting in the small peak ( $\text{V}_{\text{in}}$ ) was hidden in the major peak ( $\text{V}_{\text{out}}$ ). Overall, the rigid nature of the  $\text{V}_{\text{in}}$  species was proved.

**Catalytic Studies.** To probe the catalytic reactivities of  $\text{Ce}_{12}\text{V}_6$  clusters, we investigated the selective oxidation of 2-chloroethyl ethyl sulfide (CEES), an organosulfide chemical simulant of the toxic blistering agent mustard gas. First, we explored the efficacy of fine ceria powder and varied capping ligands as catalysts, which presented negligible reactivity toward the oxidation reaction (Figure S15). As negligible conversion in both cases was observed, the catalytic reactivity was then calculated on the basis of the V atoms herein for the sake of comparison.

The heterogeneous catalytic activity of the  $\text{Ce}_{12}\text{V}_6$  clusters was then interrogated, given the importance of catalyst separation and reusability.<sup>58,59</sup> We utilized acetonitrile as the solvent, in which the  $\text{Ce}_{12}\text{V}_6$  remains insoluble, and *tert*-butyl hydroperoxide (TBHP) as the oxidant and carried out the

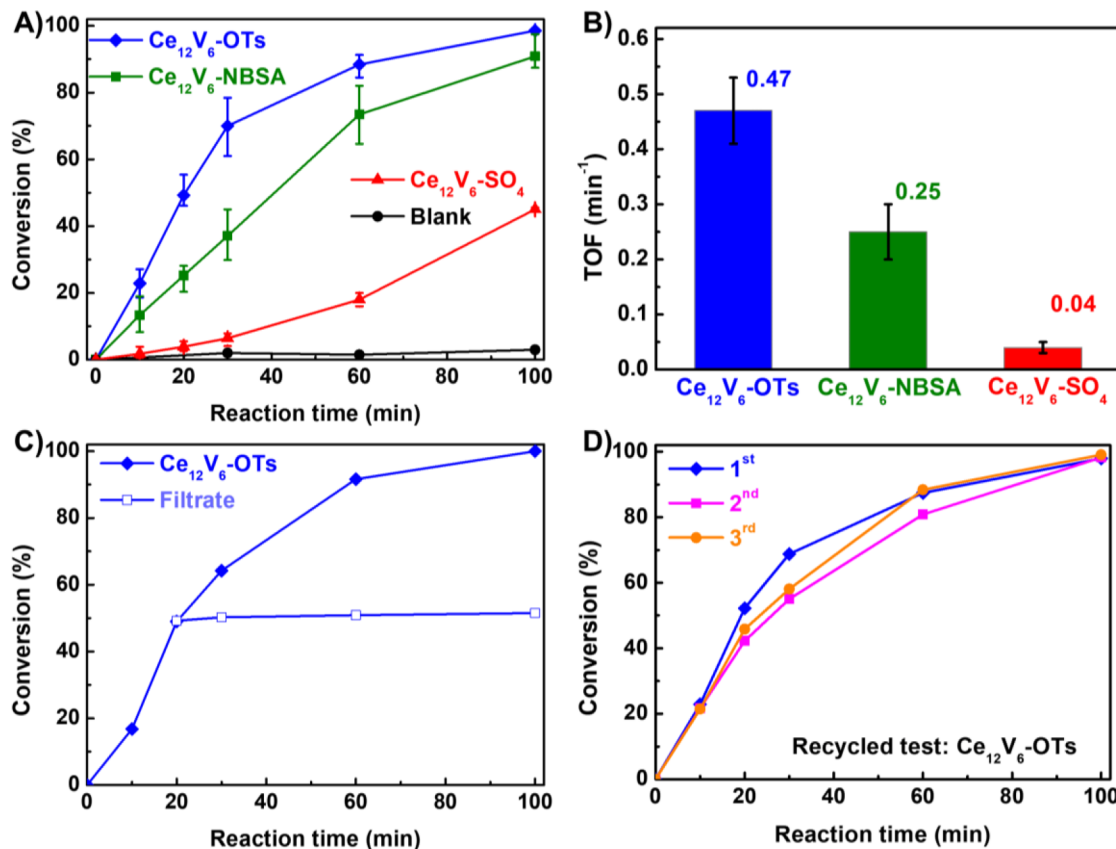


**Figure 5.** (A) Kinetic reaction plots with error bars over three trials for all clusters. (B) TOF comparison among three clusters. (C) Leaching experiment (carried out with  $\text{Ce}_{12}\text{V}_6\text{-OTs}$  after 20 min). (D) Recyclability test with  $\text{Ce}_{12}\text{V}_6\text{-OTs}$ .

reaction under 30 °C (Scheme 1). Kinetic reaction plots with all clusters are displayed in Figure 5A and Figures S16–S18. While negligible conversion was detected for the reaction without catalyst, the other reactions with  $\text{Ce}_{12}\text{V}_6$ -oxo cluster oxidized CEES. During the first 30 min of the reaction,  $\text{Ce}_{12}\text{V}_6\text{-OTs}$  exhibited the best performance with a turnover frequency (TOF, calculated on the basis of V atoms) of 0.47  $\text{min}^{-1}$ , followed by 0.25  $\text{min}^{-1}$  for  $\text{Ce}_{12}\text{V}_6\text{-NBSA}$ , and lastly  $\text{Ce}_{12}\text{V}_6\text{-SO}_4$  with the lowest TOF of 0.04  $\text{min}^{-1}$  (Figure 5B). Thus, the reactivity for  $\text{Ce}_{12}\text{V}_6\text{-OTs}$  is approximately 2 and 10 times higher than those for  $\text{Ce}_{12}\text{V}_6\text{-NBSA}$  and  $\text{Ce}_{12}\text{V}_6\text{-SO}_4$ . The higher reactivity of  $\text{Ce}_{12}\text{V}_6\text{-OTs}$  than  $\text{Ce}_{12}\text{V}_6\text{-NBSA}$  can be rationalized by the higher V 2p B.E. for  $\text{Ce}_{12}\text{V}_6\text{-OTs}$  (517.7/525.0 eV) than that for the  $\text{Ce}_{12}\text{V}_6\text{-NBSA}$  (517.1/524.4 eV) (Figure 4 and Table S4), as a higher oxidation state V species will more readily obtain electrons from the sulfur atom on the CEES molecule (Figure S19).<sup>45,60</sup> On the contrary,  $\text{Ce}_{12}\text{V}_6\text{-SO}_4$  presented the lowest catalytic performance, which can be well-explained by the poorer accessibility to the active sites in the densely packed cluster, as confirmed by both CO<sub>2</sub> and CEES adsorption data (Figure 2D and Figure S20), further highlighting the catalytic significance of the porosity introduction. Among all  $\text{Ce}_{12}\text{V}_6$  clusters, we observed a > 99% selectivity toward the singly oxidized nontoxic CEESO product. We used ICP, <sup>1</sup>H NMR, and filtrate experiments to demonstrate the heterogeneous nature of the reactions. From ICP results, the Ce/V ratio remained consistent after the reaction with negligible Ce/V content in the filtrate (Table S8). <sup>1</sup>H NMR spectra indicated identical ligands present on the pre-/postcatalysis samples (~7 TsoH and ~6 NBSA per

$\text{Ce}_{12}\text{V}_6$  core) (Figure S21). The remaining filtrate exhibited limited conversion after filtering the catalysts out from the solution (Figure 5C and Figure S22). To demonstrate the stability of the highest performing catalyst,  $\text{Ce}_{12}\text{V}_6\text{-OTs}$  was recycled and reused under the same conditions for another two times (Figure 5D), with each recycled trial exhibiting comparable conversion as compared to the pristine catalyst. Though there was an insignificant decrease in ligand loading after three recycles (<3% loss) (Figure S23), the reproducible results suggested the high stability of this catalyst. Lastly, PXRD of all postcatalysis  $\text{Ce}_{12}\text{V}_6$  samples indicated a retention in crystallinity (Figure S24).

Homogeneous catalytic reactivity was also probed by the reaction in DMF with  $\text{Ce}_{12}\text{V}_6\text{-OTs}$  as a catalyst (see the SI for more experimental details). A benchmark polyoxometalate (POM), decamolybdodivanado phosphoric acid ( $\text{H}_5\text{PV}_2\text{Mo}_{10}\text{O}_{40}$ ), where the vanadium species was also reported to be highly active for the reaction,<sup>61</sup> was applied in the same condition to show the comparison. As can be seen in Figure S25 and Table S9, while the blank experiment presents a rather low conversion of only ~11% in 60 min,  $\text{Ce}_{12}\text{V}_6\text{-OTs}$  can realize a nearly full conversion of ~90%, being similar to the  $\text{H}_5\text{PV}_2\text{Mo}_{10}\text{O}_{40}$  (~99%).

## CONCLUSIONS

In this work, we reported three isostructural highly symmetric cerium vanadium oxo clusters coordinated by sulfate groups ( $\text{Ce}_{12}\text{V}_6\text{-SO}_4$ ), toluenesulfonate groups ( $\text{Ce}_{12}\text{V}_6\text{-OTs}$ ), and nitrobenzene sulfate groups ( $\text{Ce}_{12}\text{V}_6\text{-NBSA}$ ). Following thorough structural characterization, we observed that these

three  $\text{Ce}_{12}\text{V}_6$  clusters range in porosity and V electronic character as attributed to the different coordination environment induced by the capping agents. To explore the effect of both porosity and electronic effects on the active V catalyst, we investigated the selective oxidation of an organosulfide molecule of CEES. Our results showed that  $\text{Ce}_{12}\text{V}_6\text{-OTs}$  exhibited ~2 and ~10 times higher TOF than  $\text{Ce}_{12}\text{V}_6\text{-NBSA}$  and  $\text{Ce}_{12}\text{V}_6\text{-SO}_4$ , attributed to a higher V B.E. and higher porosity. This work provides a series of soluble molecularly precise cerium vanadium oxo clusters, and we anticipate that these clusters can also serve as potent homogeneous catalysts and photocatalysts. The strategy reported herein highlights the structural and electronic tunability that capping agents can impart within a heterometallic metal oxo cluster to result in varying reactivity for heterogeneous oxidative catalysis. We anticipate that this approach will be widely applicable to introduce targeted structure and function within inorganic clusters.

## ■ ASSOCIATED CONTENT

### SI Supporting Information

The Supporting Information is available free of charge at <https://pubs.acs.org/doi/10.1021/jacs.1c11208>.

Discussions of chemicals used, experimental methods, and analytical techniques, tables of crystallographic data, ICP results, EDS results, V 2p binding energies, integration area ratios, and conversion and selectivity comparison for homogeneous catalysis, and figures of PXRD patterns, ball and stick, packing, and polyhedral modes, NMR spectra, SEM and HRTEM images, EDS linescan results, UV-vis spectra, ESI-MS spectrum, TGA curves, XPS spectra, size distribution, simulated perfect size, CEES oxidation, triplet runs of CEES oxidation, reaction mechanism of CEES oxidation, CEES adsorption, and leaching experiment ([PDF](#))

### Accession Codes

CCDC 2117154 and 2117244 contain the supplementary crystallographic data for this paper. These data can be obtained free of charge via [www.ccdc.cam.ac.uk/data\\_request/cif](http://www.ccdc.cam.ac.uk/data_request/cif), or by emailing [data\\_request@ccdc.cam.ac.uk](mailto:data_request@ccdc.cam.ac.uk), or by contacting The Cambridge Crystallographic Data Centre, 12 Union Road, Cambridge CB2 1EZ, UK; fax: +44 1223 336033.

## ■ AUTHOR INFORMATION

### Corresponding Authors

May Nyman – Department of Chemistry, Oregon State University, Corvallis, Oregon 97331, United States; [orcid.org/0000-0002-1787-0518](https://orcid.org/0000-0002-1787-0518); Email: [may.nyman@oregonstate.edu](mailto:may.nyman@oregonstate.edu)

Omar K. Farha – International Institute for Nanotechnology and Department of Chemistry, Northwestern University, Evanston, Illinois 60208, United States; Department of Chemical and Biological Engineering, Northwestern University, Evanston, Illinois 60208, United States; [orcid.org/0000-0002-9904-9845](https://orcid.org/0000-0002-9904-9845); Email: [o-farha@northwestern.edu](mailto:o-farha@northwestern.edu)

### Authors

Xingjie Wang – International Institute for Nanotechnology and Department of Chemistry, Northwestern University, Evanston, Illinois 60208, United States; [orcid.org/0000-0002-5802-9944](https://orcid.org/0000-0002-5802-9944)

Kieran Brunson – Department of Chemistry, Oregon State University, Corvallis, Oregon 97331, United States

Haomiao Xie – International Institute for Nanotechnology and Department of Chemistry, Northwestern University, Evanston, Illinois 60208, United States

Ian Colliard – Department of Chemistry, Oregon State University, Corvallis, Oregon 97331, United States

Megan C. Wasson – International Institute for Nanotechnology and Department of Chemistry, Northwestern University, Evanston, Illinois 60208, United States; [orcid.org/0000-0002-9384-2033](https://orcid.org/0000-0002-9384-2033)

Xinyi Gong – International Institute for Nanotechnology and Department of Chemistry, Northwestern University, Evanston, Illinois 60208, United States; [orcid.org/0000-0003-0295-3959](https://orcid.org/0000-0003-0295-3959)

Kaikai Ma – International Institute for Nanotechnology and Department of Chemistry, Northwestern University, Evanston, Illinois 60208, United States; [orcid.org/0000-0003-0414-4397](https://orcid.org/0000-0003-0414-4397)

Yufang Wu – International Institute for Nanotechnology and Department of Chemistry, Northwestern University, Evanston, Illinois 60208, United States; [orcid.org/0000-0001-6354-883X](https://orcid.org/0000-0001-6354-883X)

Florencia A. Son – International Institute for Nanotechnology and Department of Chemistry, Northwestern University, Evanston, Illinois 60208, United States; [orcid.org/0000-0002-7524-3774](https://orcid.org/0000-0002-7524-3774)

Karam B. Idrees – International Institute for Nanotechnology and Department of Chemistry, Northwestern University, Evanston, Illinois 60208, United States; [orcid.org/0000-0002-9603-3952](https://orcid.org/0000-0002-9603-3952)

Xuan Zhang – International Institute for Nanotechnology and Department of Chemistry, Northwestern University, Evanston, Illinois 60208, United States

Justin M. Notestein – Department of Chemical and Biological Engineering, Northwestern University, Evanston, Illinois 60208, United States; [orcid.org/0000-0003-1780-7356](https://orcid.org/0000-0003-1780-7356)

Complete contact information is available at:

<https://pubs.acs.org/10.1021/jacs.1c11208>

### Notes

The authors declare no competing financial interest.

## ■ ACKNOWLEDGMENTS

This work was supported as part of the Catalysis in Energy Processes (ICEP) for work done at Northwestern University, funded by the DOE, Office of Basic Energy Sciences (award number DE-FG02-03ER15457). M.C.W. was supported by the NSF Graduate Research Fellowship under grant DGE-1842165. F.A.S. was supported by the Department of Defense (DoD) through the National Defense Science & Engineering Graduate (NDSEG) Fellowship Program. X.G. and F.A.S. gratefully acknowledge support from the Ryan Fellowship and the International Institute for Nanotechnology at Northwestern University. K.B., I.C., and M.N. acknowledge the U.S. Department of Energy, National Nuclear Security Administration (NNSA), for work done at Oregon State University, award number DE-NA0003763, and M.N. acknowledges the Alexander von Humboldt foundation. X.W. would like to thank Jingyi Sui for providing the decamolybdochovanado phosphoric acid ( $\text{H}_5\text{PV}_2\text{Mo}_{10}\text{O}_{40}$ ). This work made use of the J.B. Cohen X-ray Diffraction Facility supported by the MRSEC program of

the National Science Foundation (DMR-1720139) at the Materials Research Center of Northwestern University. ICP-OES metal analysis was performed at the Northwestern University Quantitative Bioelement Imaging Center. This work made use of Keck-II and EPIC facilities of the NUANCE Center at Northwestern University, which has received support from the Soft and Hybrid Nanotechnology Experimental (SHyNE) Resource (NSF NNCI-1542205); the MRSEC program (NSF DMR-1720139) at the Materials Research Center; the International Institute for Nanotechnology (IIN); the Keck Foundation; and the State of Illinois, through the IIN. This work made use of the IMSERC at Northwestern University, which has received support from the NSF (CHE-1048773 and DMR-0521267), SHyNE Resource (NSF NNCI-1542205), the State of Illinois, and IIN.

## ■ REFERENCES

- (1) Goulas, K. A.; Mironenko, A. V.; Jenness, G. R.; Mazal, T.; Vlachos, D. G. Fundamentals of C–O bond activation on metal oxide catalysts. *Fundamentals of C–O bond activation on metal oxide catalysts* **2019**, *2* (3), 269–276.
- (2) Puigdollers, A. R.; Pacchioni, G. CO Oxidation on Au Nanoparticles Supported on ZrO<sub>2</sub>: Role of Metal/Oxide Interface and Oxide Reducibility. *ChemCatChem* **2017**, *9* (6), 1119–1127.
- (3) Dlugosz, O.; Szostak, K.; Staron, A.; Pulit-Prociak, J.; Banach, M. Methods for Reducing the Toxicity of Metal and Metal Oxide NPs as Biomedicine. *Materials* **2020**, *13* (2), 279.
- (4) Nikolova, M. P.; Chavali, M. S. Metal Oxide Nanoparticles as Biomedical Materials. *Metal Oxide Nanoparticles as Biomedical Materials* **2020**, *5* (2), 27.
- (5) Maier, S. A.; Brongersma, M. L.; Kik, P. G.; Meltzer, S.; Requicha, A. A.; Atwater, H. A. Plasmonics—a route to nanoscale optical devices. *Adv. Mater.* **2001**, *13* (19), 1501–1505.
- (6) Ney, A.; Pampuch, C.; Koch, R.; Ploog, K. H. Programmable computing with a single magnetoresistive element. *Nature* **2003**, *425* (6957), 485–487.
- (7) Atwater, H. A.; Polman, A. Plasmonics for improved photovoltaic devices. *Nat. Mater.* **2010**, *9* (3), 205–213.
- (8) Noginov, M. A.; Zhu, G.; Belgrave, A. M.; Bakker, R.; Shalaev, V. M.; Narimanov, E. E.; Stout, S.; Herz, E.; Suteewong, T.; Wiesner, U. Demonstration of a spaser-based nanolaser. *Nature* **2009**, *460* (7259), 1110–1112.
- (9) Jing, L.; Zhou, W.; Tian, G.; Fu, H. Surface tuning for oxide-based nanomaterials as efficient photocatalysts. *Chem. Soc. Rev.* **2013**, *42* (24), 9509–9549.
- (10) Huang, M. H.; Rej, S.; Chiu, C. Y. Facet-Dependent Optical Properties Revealed through Investigation of Polyhedral Au-Cu<sub>2</sub>O and Bimetallic Core-Shell Nanocrystals. *Small* **2015**, *11* (23), 2716–2726.
- (11) Rothschild, A.; Komem, Y. The effect of grain size on the sensitivity of nanocrystalline metal-oxide gas sensors. *J. Appl. Phys.* **2004**, *95* (11), 6374–6380.
- (12) Lane, M. K. M.; Zimmerman, J. B. Controlling metal oxide nanoparticle size and shape with supercritical fluid synthesis. *Green Chem.* **2019**, *21* (14), 3769–3781.
- (13) Wu, Z.; Li, M.; Overbury, S. H. On the structure dependence of CO oxidation over CeO<sub>2</sub> nanocrystals with well-defined surface planes. *J. Catal.* **2012**, *285* (1), 61–73.
- (14) Li, Z.; Ji, S.; Liu, Y.; Cao, X.; Tian, S.; Chen, Y.; Niu, Z.; Li, Y. Well-Defined Materials for Heterogeneous Catalysis: From Nanoparticles to Isolated Single-Atom Sites. *Chem. Rev.* **2020**, *120* (2), 623–682.
- (15) Liu, J. X.; Gao, M. Y.; Fang, W. H.; Zhang, L.; Zhang, J. Bandgap Engineering of Titanium-Oxo Clusters: Labile Surface Sites Used for Ligand Substitution and Metal Incorporation. *Angew. Chem., Int. Ed.* **2016**, *55* (17), 5160–5165.
- (16) Chen, W.-P.; Liao, P.-Q.; Jin, P.-B.; Zhang, L.; Ling, B.-K.; Wang, S.-C.; Chan, Y.-T.; Chen, X.-M.; Zheng, Y.-Z. The Gigantic {Ni<sub>36</sub>Gd<sub>102</sub>} Hexagon: A Sulfate-Templated “Star-of-David” for Photocatalytic CO<sub>2</sub> Reduction and Magnetic Cooling. *J. Am. Chem. Soc.* **2020**, *142* (10), 4663–4670.
- (17) Wasson, M. C.; Zhang, X.; Otake, K.-i.; Rosen, A. S.; Alayoglu, S.; Krzyzaniak, M. D.; Chen, Z.; Redfern, L. R.; Robison, L.; Son, F. A.; Chen, Y.; Islamoglu, T.; Notestein, J. M.; Snurr, R. Q.; Wasielewski, M. R.; Farha, O. K. Supramolecular Porous Assemblies of Atomically Precise Catalytically Active Cerium-Based Clusters. *Chem. Mater.* **2020**, *32* (19), 8522–8529.
- (18) Smolders, S.; Jacobsen, J.; Stock, N.; De Vos, D. Selective catalytic reduction of NO by cerium-based metal-organic frameworks. *Catal. Sci. Technol.* **2020**, *10* (2), 337–341.
- (19) Chen, X.; Chen, X.; Yu, E.; Cai, S.; Jia, H.; Chen, J.; Liang, P. In situ pyrolysis of Ce-MOF to prepare CeO<sub>2</sub> catalyst with obviously improved catalytic performance for toluene combustion. *Chem. Eng. J.* **2018**, *344*, 469–479.
- (20) Samek, I. A.; Bobbitt, N. S.; Snurr, R. Q.; Stair, P. C. Structure and activity of mixed VOx-CeO<sub>2</sub> domains supported on alumina in cyclohexane oxidative dehydrogenation. *J. Catal.* **2020**, *384*, 147–158.
- (21) Paier, J.; Penschke, C.; Sauer, J. Oxygen defects and surface chemistry of ceria: quantum chemical studies compared to experiment. *Chem. Rev.* **2013**, *113* (6), 3949–3985.
- (22) Agasti, N.; Astle, M. A.; Rance, G. A.; Alves Fernandes, J.; Dupont, J.; Khlobystov, A. N. Cerium Oxide Nanoparticles Inside Carbon Nanoreactors for Selective Allylic Oxidation of Cyclohexene. *Nano Lett.* **2020**, *20* (2), 1161–1171.
- (23) Wang, Y.; Arandiyani, H.; Scott, J.; Bagheri, A.; Dai, H.; Amal, R. Recent advances in ordered meso/macroporous metal oxides for heterogeneous catalysis: a review. *J. Mater. Chem. A* **2017**, *5* (19), 8825–8846.
- (24) Liu, L.; Corma, A. Metal Catalysts for Heterogeneous Catalysis: From Single Atoms to Nanoclusters and Nanoparticles. *Chem. Rev.* **2018**, *118* (10), 4981–5079.
- (25) Shirase, S.; Tamaki, S.; Shinohara, K.; Hirosawa, K.; Tsurugi, H.; Satoh, T.; Mashima, K. Cerium (IV) Carboxylate Photocatalyst for Catalytic Radical Formation from Carboxylic Acids: Decarboxylative Oxygenation of Aliphatic Carboxylic Acids and Lactonization of Aromatic Carboxylic Acids. *J. Am. Chem. Soc.* **2020**, *142* (12), 5668–5675.
- (26) Abanades, S.; Flamant, G. Thermochemical hydrogen production from a two-step solar-driven water-splitting cycle based on cerium oxides. *Sol. Energy* **2006**, *80* (12), 1611–1623.
- (27) Lu, Y.; Zhu, L.; Agrafiotis, C.; Vieten, J.; Roeb, M.; Sattler, C. Solar fuels production: Two-step thermochemical cycles with cerium-based oxides. *Prog. Energy Combust. Sci.* **2019**, *75*, 100785.
- (28) Scheffe, J. R.; Steinfeld, A. Thermodynamic Analysis of Cerium-Based Oxides for Solar Thermochemical Fuel Production. *Energy Fuels* **2012**, *26* (3), 1928–1936.
- (29) Dhall, A.; Self, W. Cerium Oxide Nanoparticles: A Brief Review of Their Synthesis Methods and Biomedical Applications. *Antioxidants* **2018**, *7* (8), 97.
- (30) Qi, M.; Li, W.; Zheng, X.; Li, X.; Sun, Y.; Wang, Y.; Li, C.; Wang, L. Cerium and Its Oxidant-Based Nanomaterials for Antibacterial Applications: A State-of-the-Art Review. *Front. Mater.* **2020**, *7*, 213.
- (31) Zhang, M.; Zhang, C.; Zhai, X.; Luo, F.; Du, Y.; Yan, C. Antibacterial mechanism and activity of cerium oxide nanoparticles. *Antibacterial mechanism and activity of cerium oxide nanoparticles* **2019**, *62* (11), 1727–1739.
- (32) Wang, H.; Zhou, H.; Li, S.; Ge, X.; Wang, L.; Jin, Z.; Wang, C.; Ma, J.; Chu, X.; Meng, X.; Zhang, W.; Xiao, F.-S. Strong Oxide-Support Interactions Accelerate Selective Dehydrogenation of Propane by Modulating the Surface Oxygen. *ACS Catal.* **2020**, *10* (18), 10559–10569.
- (33) Li, S.; Xu, Y.; Chen, Y.; Li, W.; Lin, L.; Li, M.; Deng, Y.; Wang, X.; Ge, B.; Yang, C.; Yao, S.; Xie, J.; Li, Y.; Liu, X.; Ma, D. Tuning the Selectivity of Catalytic Carbon Dioxide Hydrogenation over Iridium/

- Cerium Oxide Catalysts with a Strong Metal-Support Interaction. *Angew. Chem., Int. Ed.* **2017**, *56* (36), 10761–10765.
- (34) Kugai, J.; Miller, J. T.; Guo, N.; Song, C. Oxygen-enhanced water gas shift on ceria-supported Pd-Cu and Pt-Cu bimetallic catalysts. *J. Catal.* **2011**, *277* (1), 46–53.
- (35) Vecchietti, J.; Bonivardi, A.; Xu, W.; Stacchiola, D.; Delgado, J.; Calatayud, M.; Collins, S. E. Understanding the Role of Oxygen Vacancies in the Water Gas Shift Reaction on Ceria-Supported Platinum Catalysts. *ACS Catal.* **2014**, *4* (6), 2088–2096.
- (36) Wang, G. C.; Sung, H. H.; Dai, F. R.; Chiu, W. H.; Wong, W. Y.; Williams, I. D.; Leung, W. H. Heterometallic cerium(IV) perrhenate, permanganate, and molybdate complexes supported by the imidodiphosphinate ligand [N(i-Pr<sub>2</sub>PO)<sub>2</sub>]. *Inorg. Chem.* **2013**, *52* (5), 2556–2563.
- (37) Weiss, C. J.; Marks, T. J. Organo-f-element catalysts for efficient and highly selective hydroalkoxylation and hydrothiolation. *Organo-f-element catalysts for efficient and highly selective hydroalkoxylation and hydrothiolation* **2010**, *39* (29), 6576–6588.
- (38) Tasiopoulos, A. J.; Wernsdorfer, W.; Moulton, B.; Zaworotko, M. J.; Christou, G. Template Synthesis and Single-Molecule Magnetism Properties of a Complex with Spin S = 16 and a [Mn<sub>8</sub>O<sub>8</sub>]<sup>8+</sup> Saddle-Like Core. *J. Am. Chem. Soc.* **2003**, *125* (50), 15274–15275.
- (39) Nishio, M.; Inami, S.; Hayashi, Y. Early-Lanthanide Complexes with All-Inorganic Macroyclic Polyoxovanadate Ligands. *Eur. J. Inorg. Chem.* **2013**, *2013* (10–11), 1876–1881.
- (40) Liu, D.; Lu, Y.; Tan, H.-Q.; Wang, T.-T.; Wang, E.-B. Series of Organic-Inorganic Hybrid Rare Earth Derivatives Based on [MnV<sub>13</sub>O<sub>38</sub>]<sup>7-</sup> Polyoxoanion: Syntheses, Structures, and Magnetic and Electrochemical Properties. *Cryst. Growth Des.* **2015**, *15* (1), 103–114.
- (41) Ober, P.; Rogg, S.; Hess, C. Direct Evidence for Active Support Participation in Oxide Catalysis: Multiple Operando Spectroscopy of VO<sub>x</sub>/Ceria. *ACS Catal.* **2020**, *10* (5), 2999–3008.
- (42) El-Korso, S.; Bedrane, S.; Choukchou-Braham, A.; Bachir, R. The effect of redox properties of ceria-supported vanadium oxides in liquid phase cyclohexene oxidation. *RSC Adv.* **2015**, *5* (78), 63382–63392.
- (43) Kropp, T.; Paier, J.; Sauer, J. Support effect in oxide catalysis: methanol oxidation on vanadia/ceria. *J. Am. Chem. Soc.* **2014**, *136* (41), 14616–14625.
- (44) Abbott, H. L.; Uhl, A.; Baron, M.; Lei, Y.; Meyer, R. J.; Stacchiola, D. J.; Bondarchuk, O.; Shaikhutdinov, S.; Freund, H. J. Relating methanol oxidation to the structure of ceria-supported vanadia monolayer catalysts. *J. Catal.* **2010**, *272* (1), 82–91.
- (45) Wong, K. L.; So, Y. M.; Wang, G. C.; Sung, H. H.; Williams, I. D.; Leung, W. H. Heterobimetallic cerium(iv) oxo clusters supported by a tripodal oxygen ligand. *Heterobimetallic cerium(iv) oxo clusters supported by a tripodal oxygen ligand* **2016**, *45* (21), 8770–8776.
- (46) Seliverstov, A.; Streb, C. Chirality meets visible-light photocatalysis in a molecular cerium vanadium oxide cluster. *Chem. Commun.* **2014**, *50* (15), 1827–1829.
- (47) Yoshida, J.-i.; Sugawara, M.; Imagawa, M. The Mechanism of the C-S Bond Cleavage in Electron Transfer Reactions of  $\alpha$ -Organothio-Substituted Heteroatom Compounds. In *Novel Trends in Electroorganic Synthesis*, Tokyo; Torii, S., Ed.; Springer Japan: Tokyo, Japan, 1998; pp 69–70.
- (48) Efremova, O. A.; Vorotnikov, Y. A.; Brylev, K. A.; Vorotnikova, N. A.; Novozhilov, I. N.; Kuratieva, N. V.; Edeleva, M. V.; Benoit, D. M.; Kitamura, N.; Mironov, Y. V.; Shestopalov, M. A.; Sutherland, A. J. Octahedral molybdenum cluster complexes with aromatic sulfonate ligands. *Octahedral molybdenum cluster complexes with aromatic sulfonate ligands* **2016**, *45* (39), 15427–15435.
- (49) Clarkson, J.; Ewen Smith, W. A DFT analysis of the vibrational spectra of nitrobenzene. *J. Mol. Struct.* **2003**, *655* (3), 413–422.
- (50) He, H.-T.; Xing, L.-C.; Zhang, J.-S.; Tang, M. Binding characteristics of Cd<sup>2+</sup>, Zn<sup>2+</sup>, Cu<sup>2+</sup>, and Li<sup>+</sup> with humic substances: Implication to trace element enrichment in low-rank coals. *Energy Explor. Exploit.* **2016**, *34* (5), 735–745.
- (51) Pelzer, K. M.; Cheng, L.; Curtiss, L. A. Effects of Functional Groups in Redox-Active Organic Molecules: A High-Throughput Screening Approach. *J. Phys. Chem. C* **2017**, *121* (1), 237–245.
- (52) Morales, J.; Espinos, J. P.; Caballero, A.; Gonzalez-Elipe, A. R.; Mejias, J. A. XPS Study of Interface and Ligand Effects in Supported Cu<sub>2</sub>O and CuO Nanometric Particles. *J. Phys. Chem. B* **2005**, *109* (16), 7758–7765.
- (53) Ashbrook, S. E.; Dawson, D. M.; Gan, Z.; Hooper, J. E.; Hung, I.; Macfarlane, L. E.; McKay, D.; McLeod, L. K.; Walton, R. I. Application of NMR Crystallography to Highly Disordered Templated Materials: Extensive Local Structural Disorder in the Gallophosphate GaPO-34A. *Inorg. Chem.* **2020**, *59* (16), 11616–11626.
- (54) Forster, J.; Rösner, B.; Fink, R. H.; Nye, L. C.; Ivanovic-Burmazovic, I.; Kastner, K.; Tucher, J.; Streb, C. Oxidation-driven self-assembly gives access to high-nucularity molecular copper vanadium oxide clusters. *Oxidation-driven self-assembly gives access to high-nucularity molecular copper vanadium oxide clusters* **2013**, *4* (1), 418–424.
- (55) Seliverstov, A.; Streb, C. A new class of homogeneous visible-light photocatalysts: molecular cerium vanadium oxide clusters. *Chem. - Eur. J.* **2014**, *20* (31), 9733–8.
- (56) Hatton, J. V.; Richards, R. E. Solvent effects in N.M.R. spectra of amide solutions. *Mol. Phys.* **1962**, *5* (2), 139–152.
- (57) Żuchowski, G.; Zborowski, K. The influence of solvent molecules on NMR spectrum of barbituric acid in the DMSO solution. *influence of solvent molecules on NMR spectrum of barbituric acid in the DMSO solution* **2006**, *4* (3), 523–532.
- (58) Shende, V. S.; Sapta, V. B.; Bhanage, B. M. Recent Advances Utilized in the Recycling of Homogeneous Catalysis. *Chem. Rec.* **2019**, *19* (9), 2022–2043.
- (59) Shende, V. S.; Sapta, V. B.; Bhanage, B. M. Recent advances utilized in the recycling of homogeneous catalysis. *Chem. Rec.* **2019**, *19* (9), 2022–2043.
- (60) Villalobos, L.; Barker Paredes, J. E.; Cao, Z.; Ren, T. tert-Butyl hydroperoxide oxygenation of organic sulfides catalyzed by diruthenium(II, III) tetracarboxylates. *Inorg. Chem.* **2013**, *52* (21), 12545–12552.
- (61) Buru, C. T.; Wasson, M. C.; Farha, O. K. H<sub>5</sub>PV<sub>2</sub>Mo<sub>10</sub>O<sub>40</sub> Polyoxometalate Encapsulated in NU-1000 Metal-Organic Framework for Aerobic Oxidation of a Mustard Gas Simulant. *ACS Appl. Nano Mater.* **2020**, *3* (1), 658–664.